Integration of strong oxide-support interaction and mesoporous confinement to engineer efficient and durable Zr/Al_2O_3 for catalytic solvent regeneration in CO_2 capture

Zhen Chen, Lei Xing, Guoxiong Zhan, Zhoulan Huang, Xinhao Bai, Rong Wang, Yue Peng, Junhua Li [*]

State Key Joint Laboratory of Environment Simulation and Pollution Control, School of Environment, Tsinghua University, Beijing 100084, PR China

ARTICLE INFO

ABSTRACT

Integration of mesoporous confinement effect and strong metal oxide-support interaction, durable and efficient Zr/Al_2O_3 catalysts were proposed to boost the carbamate regeneration dynamics. The catalytic performance of powder and pelletized Zr/Al_2O_3 catalysts was verified and comprehensively evaluated according to lab-scale and bench-scale setup, while the promotion mechanism was explored based on characterization analysis and theoretical calculation. The maximum rate of carbamate decomposition (or CO_2 desorption) using powder Zr/Al_2O_3 increased by 178% compared to the catalyst-free case, resulting in approximately 27% lower relative heat duty. Bench-scale testing (11 hours) with continuous CO_2 absorption and desorption demonstrated an optimal capture efficiency of 54.2% with pelletized Zr/Al_2O_3, increased by 12.5% higher than the blank case. A 4-weeks hydrothermal testing indicated that the catalysts had minimal impact on solvent degradation. This work demonstrates a feasible strategy of utilizing mesoporous soild acid material to realize the energy-efficient slovent regeneration during amined-based CO_2 capture.

1. Introduction

The global concern over the carbon dioxide (CO_2) emissions from industrial fossil fuel consumption has led to the development of chemical-absorption capture technologies [1–3]. These technologies, based on the rapid zwitterion-mediated reaction involving amine solvents and CO_2, offer a promising and viable means to reduce industrial carbon emissions and establish a carbon-neutral process [4–6]. The fast reaction rate between CO_2 and amine solvents enhances CO_2 absorption efficiency, but efficient solvent regeneration (carbamate decomposition) requires operation at high temperatures, typically above 110 °C [7–9]. The CO_2 desorption, or amine regeneration, in this reversible process, is governed by protonation and deprotonation reactions, which have an enthalpy of up to 84.3 kJ/mol for monoethanolamine (MEA) solvents [10–12]. Consequently, high-enthalpy steam is typically needed to provide energy for solvent regeneration, primarily due to the high sensible and latent heat consumption of solvent water, which can reach up to 70% [13–15]. High regeneration temperature leads to significant energy penalties and accelerates solvent loss through oxidation or thermal degradation [16,17]. As a result, the urgent need for the development of energy-efficient and eco-friendly carbon capture technologies is emphasized on an industrial scale.

Recently, the use of solid acid catalysts (SAC) for solvent regeneration has gained attention as a promising approach to reduce energy consumption [18–21]. This is achieved by enhancing the key processes of proton transfer and breaking C–N bonds during carbamate decomposition; these introduced catalysts enable efficient CO_2 desorption using a suitably lean solvent at relatively low operating pressure and temperature [22–24]. If the rich solvent can be catalytically regenerated at relatively temperature, it could pave a possible way to using lower-grade heat sources or significantly improve the heat utilization efficiency during solvent regeneration [7,18]. The amine regeneration process can be theoretically described as reversible amine zwitterions, where proton transfer (H^+, H_3O^+, and RNH_3^+) plays a crucial role in carbamate decomposition [3,23]. However, proton transfer is significantly hindered by the alkaline nature of the amine-based solvent. Additionally, the stability of acidic active sites on catalysts is easily affected by alkaline solvents [25,26]. The impact of dissolved elements

in the solution on amine degradation during long-term operation remains unknown. Therefore, it remains a significant challenge to develop practical solid acid catalysts with both excellent activity and durability for catalytic solvent regeneration.

Among various structures, mesoporous materials with adjustable crystal structure and morphology are particularly appealing as functional supports [27–29]. Mesoporous metallic oxide supports, in particular, offer distinct advantages in terms of feasibility, stability, and cost-effectiveness, compared to reported molecular sieves and metal/-covalent organic framework supports [30–32]. Utilizing mesoporous supports, the approach of designing composite metal oxides has proven effective in enhancing acidity, primarily due to the electronegativity differences among various metallic elements [33,34]. Furthermore, the engineering of a strong metal-oxide support interaction (SOSI) has garnered significant attention for its remarkable potential in creating advanced materials with unique catalytic performance [35,36]. Notably, the redistribution of electrons at the interface between metal oxide nanoparticles (NPs) and supports can influence electron transfer mechanisms and generate active sites, including Brønsted acid sites (BASs) and Lewis acid sites (LASs), which accelerate carbamate decomposition [10,37]. Using mesoporous supports, mesoporous confinement (MPC) can prevent the aggregation of loaded NPs, offering ample opportunities for achieving a high surface area and a stable structure [38,39]. Thus, the fabrication of active and durable metal oxide NPs anchored within mesoporous materials, along with an understanding of the role of this structure in facilitating heterogeneous proton transfer, are crucial for achieving energy-efficient and long-lasting catalytic CO_2 desorption.

In this study, a simple approach to create mesoporous hybrid materials by incorporating ZrO_2 nanoparticles into honeycomb-like mesoporous γ-Al_2O_3 is presented (referred to as Zr/Al_2O_3). A method guided by surfactants and block copolymers as templates is employed to produce highly ordered pores. ZrO_2 was anchored over the mesoporous support through mild hydrolysis. The structural information at the interface of nanoparticle-support is described in detail, based on atomic-level morphology observations. The physical/chemical properties and coordination environment were characterized using various measurements. Catalytic performance was comprehensively evaluated using a MEA solvent saturated with CO_2. To verify the catalytic performance of pelletized Zr/Al_2O_3 catalysts, a bench-scale continuous CO_2 absorption-desorption (BCCAD) system is designed. The reciprocal effect between catalysts and solvent was explored through an extended hydrothermal testing period. Additionally, we attempt to propose a plausible mechanism for proton transfer to elucidate the role of solid acid in the regeneration of amine-based solvents.

2. Experimental and methodology

2.1. Materials and preparation

The chemicals were purchased from Shanghai Macklin Biochemical Co., Ltd. (China) and used without additional purification: aluminum nitrate nonahydrate ($Al(NO_3)_3 \cdot 9H_2O$, 99%), zirconium propoxide solution ($Zr(OPr-n)_4$, 70 wt%), zirconium(IV) dioxide (50 nm ZrO_2, 99.99%), sodium chloride (NaCl, 99.5%), polyethylene-polypropylene glycol (P123, average Mn=~5800), ammonium hydroxide solution (NH_4OH, 25–28 wt%), monoethanolamine (MEA, 99%), Ethanol (ET, 99.5%) and pyridine (Py, 99.7%).

Mesoporous γ-Al_2O_3 was prepared using a sol-gel process, employing a nonionic block copolymer (P123) as a template in ethanol solvent [38, 40]. The mixture of γ-Al_2O_3 and Zr precursor ($Zr(OPr-n)_4$) underwent complete hydrolysis and was subsequently calcined to create powder Zr/Al_2O_3 catalysts for laboratory-scale experiments (Figure S1a). For bench-scale experiments, gamma-phase aluminum oxide pellets (λ-Al_2O_3, ø 3 mm AR 99%, Alfa Aesar Co., Ltd.) were utilized to prepare pelletized Zr/Al_2O_3 following similar methods to loading ZrO_2

(Figure S1b). More detailed information on the material synthesis can be found in the Supporting Information (SI).

2.2. Characterization and calculations

The catalyst was examined through a combination of theoretical and experimental investigations, encompassing an exploration of its physical characteristics, chemical properties, and structure. Various analytical techniques were employed, including X-ray diffraction (XRD), N_2 adsorption-desorption, scanning electron microscopy (SEM), and transmission electron microscopy (TEM) at varying resolutions. Elemental composition was determined via energy-dispersive X-ray spectroscopy (EDX) and inductively coupled plasma-optical emission spectroscopy (ICP). Surface properties were elucidated through ammonia temperature-programmed desorption (NH_3-TPD) and pyridine-adsorption infrared (Py-IR) analysis, which allowed for the investigation of acid sites. Insights into electronic interaction and bonding were gleaned using X-ray photoelectron spectroscopy (XPS), nuclear magnetic resonance (NMR), and Raman spectra. Furthermore, X-ray absorption fine structure (XAFS) spectra were analyzed to comprehend the coordination environments. Density functional theory (DFT) calculations, employing the VASP 5.4.4 software package, were conducted to explore the electron transfer and catalytic reaction mechanism. The crystal structure and terminal surface of Al_2O_3 substrate and doped Zr atom was established by characterization results. The arranged hydroxyls and exposed metal atoms was treated as Brønsted acid sites (BASs) and the Lewis acid sites (LASs), respectively. The electron transfer scheme was analyzed by the results of charge density difference, electronic localization function (ELF), Bader charge and density of state (DOS). Specific condition and parameters of characterization and calculations were provided in the SI.

2.3. Performance evaluation

To assess the catalytic performance, CO_2 desorption from a CO_2-saturated MEA solvent (30 wt%) in a batch reactor, following specific heating profiles (Figure S2). Initially, the 5 M MEA (~30 wt%) solvent a 100 mL three-necks flask was saturated with pure CO_2 (200 mL/min) at 40 °C, to prepare a CO_2-saturated solvent. During this step, CO_2 reacted with MEA to produce protonated amine (RNH_3^+) and carbamate ($RNHCOO^-$). Subsequently, the RNH_3^+ and $RNHCOO^-$ were regenerated into MEA molecules under heating conditions (from 40 to 90 °C), enabling the evaluation of the prepared materials' catalytic performance. The desorbed CO_2 was diluted with an additional N_2 flow (200 mL/min), and the concentration of mixture flow was measured by infrared (IR) gas analyzer (MKS and IGS). According to the instantaneous concentration (C, %) of desorbed CO_2 carried by N_2 flow (200 mL/min), the desorption rate (r_d, mmol/min) could be determined by Eq. 1.

To further verify the catalytic performance of the pelletized Zr/Al_2O_3 catalysts, a bench-scale continuous CO_2 absorption-desorption (BCCAD) system was designed and built. This system was exposed to a simulated flue gas with 12 vol% CO_2 at a flow rate of 800 mL/min, as shown in Figure S3. Typically, 200 mL 5 M MEA solvent (30 wt%) successively injects into two reactors. After solvent was heated to specified temperature, the simulated flue gas with 12 vol% CO_2 (800 mL/min) switched to absorption reactor for CO_2 capture. The cyclic flow of solvent was set at 15 mL/min, with liquid-to-gas ratio at 18.75. The absorption and desorption temperature was set at 44 °C and 97 °C (atmospheric pressure), respectively. The heating temperature of oil bath before stripper was set at 100 °C. Absorbent sampling points were arranged at the outlet of reactors, for intermittently measuring the CO_2 loading. CO_2 concentration profiles were measured using an infrared (IR) gas analyzer (MKS and IGS) to evaluate various parameters, including desorption rate (r_d, mmol/min), desorbed CO_2 amount, heat duty (H, kJ/mol), and capture efficiency. Furthermore, a long-term durability test spanning weeks was conducted to investigate the impact of the catalysts on the MEA solvent,

including CO_2 loading and degradation processes. Detailed information on the performance evaluation can be found in the SI.

$$r_d = \frac{200C}{22.4(1-C)} \tag{1}$$

$$\eta = 1 - \frac{Q^0_{mix} - Q^0_{CO_2}}{Q^0_{mix}} \cdot \frac{C^t_{CO_2}}{\left(1 - C^t_{CO_2}\right)C^0_{CO_2}} \tag{2}$$

3. Results and discussions

3.1. Structure and morphology

The synthesis of Zr/Al_2O_3 catalysts comprises two steps. First,

mesoporous γ-Al_2O_3 is prepared using a template method, followed by the anchoring of Zr clusters onto the Al support through the hydrolysis of $Zr(OPr\text{-}n)_4$ and subsequent calcination treatment (Fig. 1a). This mesoporous alumina serves as the support for loading zirconia nanoparticles (NPs) to create acid catalysts with both high activity and stability. This is achieved through the strong oxide-support interaction (SOSI) and mesoporous confinement (MPC) effect. The typical TEM image of the γ-Al_2O_3 (Fig. 1b) revealed a honeycomb-like framework in a large domain. Some of the crystalline ZrO_2 was derived from the walls of the alumina support and forms nanoparticles (Fig. 1c), with average size at ~5.6 nm. High-resolution TEM (HRTEM) image (Fig. 1d) confirmed the uniform (111) growth of zirconia particles, likely originated from the inner wall of Al_2O_3 pore. As results, the size of zirconia particles was closed to that of mesopores, due to confinement effect. An atom-scale
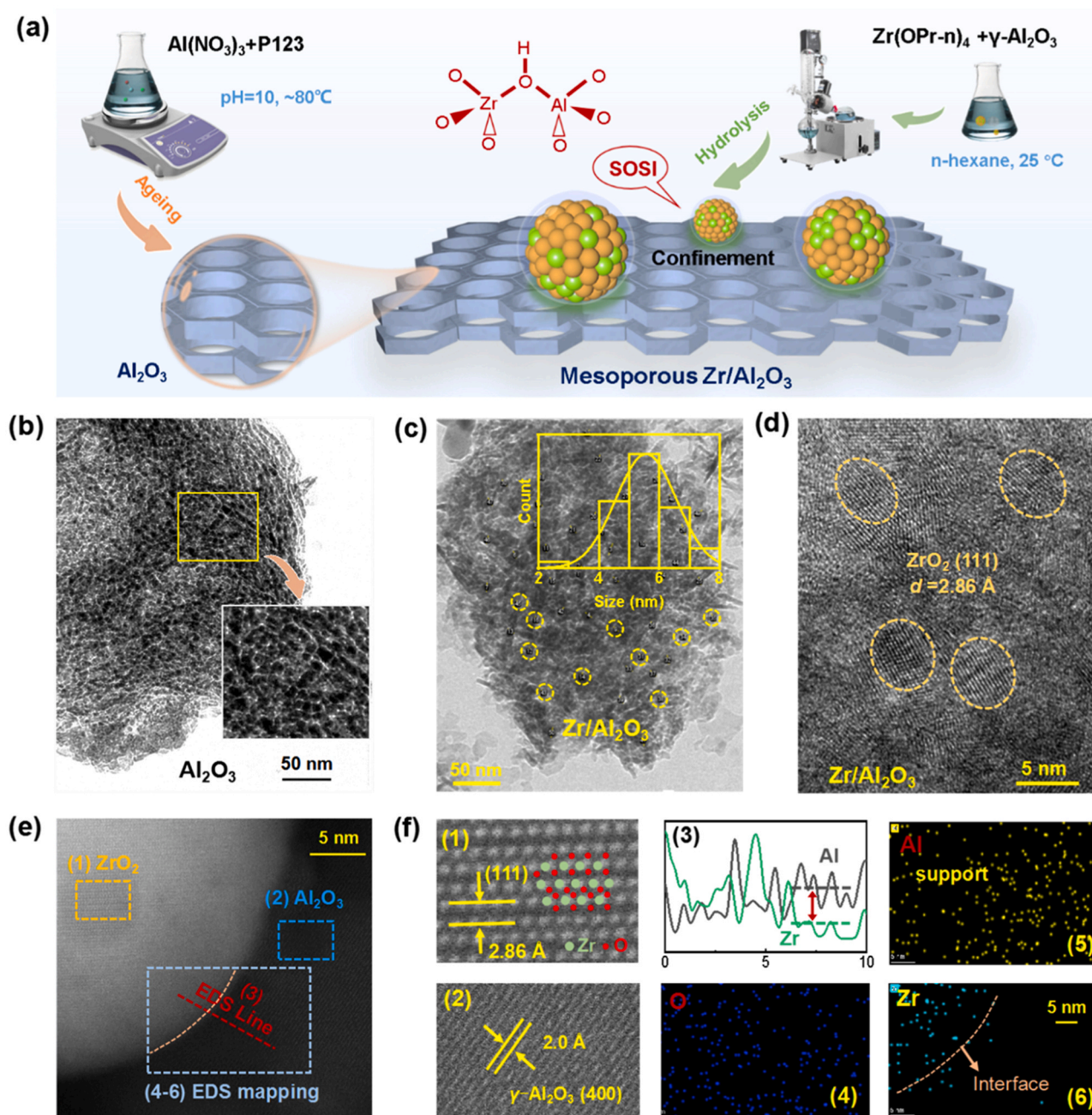

Fig. 1. Morphology and textural characterization of the as-prepared catalysts. (a) Schematic illustration of the synthesis of as-prepared materials. (b-c) TEM images of the γ-Al_2O_3 support and Zr/Al_2O_3 catalysts. (d) High-resolution TEM image. (e) HAADF-STEM image and EDS reports, including: (f1-f2) Lattice spacing of metallic oxides, (f3) EDS line scanning, and (f4-f6) elemental mapping.

high-angle annular dark-field scanning TEM (HAADF-STEM) image (Fig. 1e) revealed the atomic-scale interfacial characteristics of the Zr/Al$_2$O$_3$ catalyst. A distinct boundary separated the bright and dark regions. Fast Fourier transform patterns (FTP) indicated that the lattice spacing in the bright region was approximately 2.86 Å, corresponding to the (111) facets of ZrO$_2$ (Fig. 1f1) [33]. In contrast, the substrate λ-Al$_2$O$_3$ exhibited an exposed (400) plane with a lattice spacing of about 2.0 Å in the dark region (Fig. 1f2) [39]. The distribution of Al and Zr elements was investigated through energy dispersive spectroscopy (EDS) line scanning across the interface (Fig. 1f3). The intensity of the Al signal was noticeably higher than that of the Zr signal in the dark region. As expected, EDS elemental mapping (blue squares in Fig. 1e) images confirmed this spatial distribution, showing a relative accumulation of Zr in the bright region and uniform dispersion of Al and O in the entire region (the support) (Fig. 1f4–1f6). These observations on the morphology validate that the alumina support with a mesoporous structure could contribute to an MC effect.

In practical applications, using submicron-sized powder catalysts could lead to the obstruction of solvent flow, making them unsuitable for real-world use. Instead, a pelletized Zr/Al$_2$O$_3$ catalyst was prepared using a similar method. These pelletized catalysts, in the form of γ-Al$_2$O$_3$ (ø 3 mm), could be effectively employed as fillers in a bench-scale stripper setup (Figure S4), the structure and morphology of which would be described in the section of bench-scale experiments.

3.2. Physical and chemical characteristics

In the wide-angle X-ray diffraction (XRD) spectrum displayed in Fig. 2a, we observed narrow peaks at 45.9° and 67° (2θ), which were identified as the (400) and (440) planes, respectively, of γ-Al$_2$O$_3$ (PDF#10-0425) [41]. This XRD spectrum confirmed the successful preparation of crystalline alumina and indicated that the Zr/Al$_2$O$_3$ catalyst retained the textural characteristics of the alumina. The broader peak around 30° (2θ) was attributed to the combined effect of the (311) plane of the Al$_2$O$_3$ support and the (–111) and (111) exposed planes of the coated ZrO$_2$ (at 28.2° and 31.5°, respectively; PDF#86-1449) [42]. The N$_2$ adsorption-desorption isotherms (Fig. 2b) for both the alumina support and Zr/Al$_2$O$_3$ exhibited typical type-IV curves with a clear hysteresis loop at high partial pressure ($P/P_0 > 0.5$). Specifically, the isotherm for the alumina support displayed a type-H1 hysteresis loop with additional uptake at $P/P_0 = 0.5$–0.95 and a steep capillary condensation step, providing further evidence of the support's mesoporosity. In line with the morphology characterization, we observed confined zirconia nanoparticles occupying the mesopores of the alumina
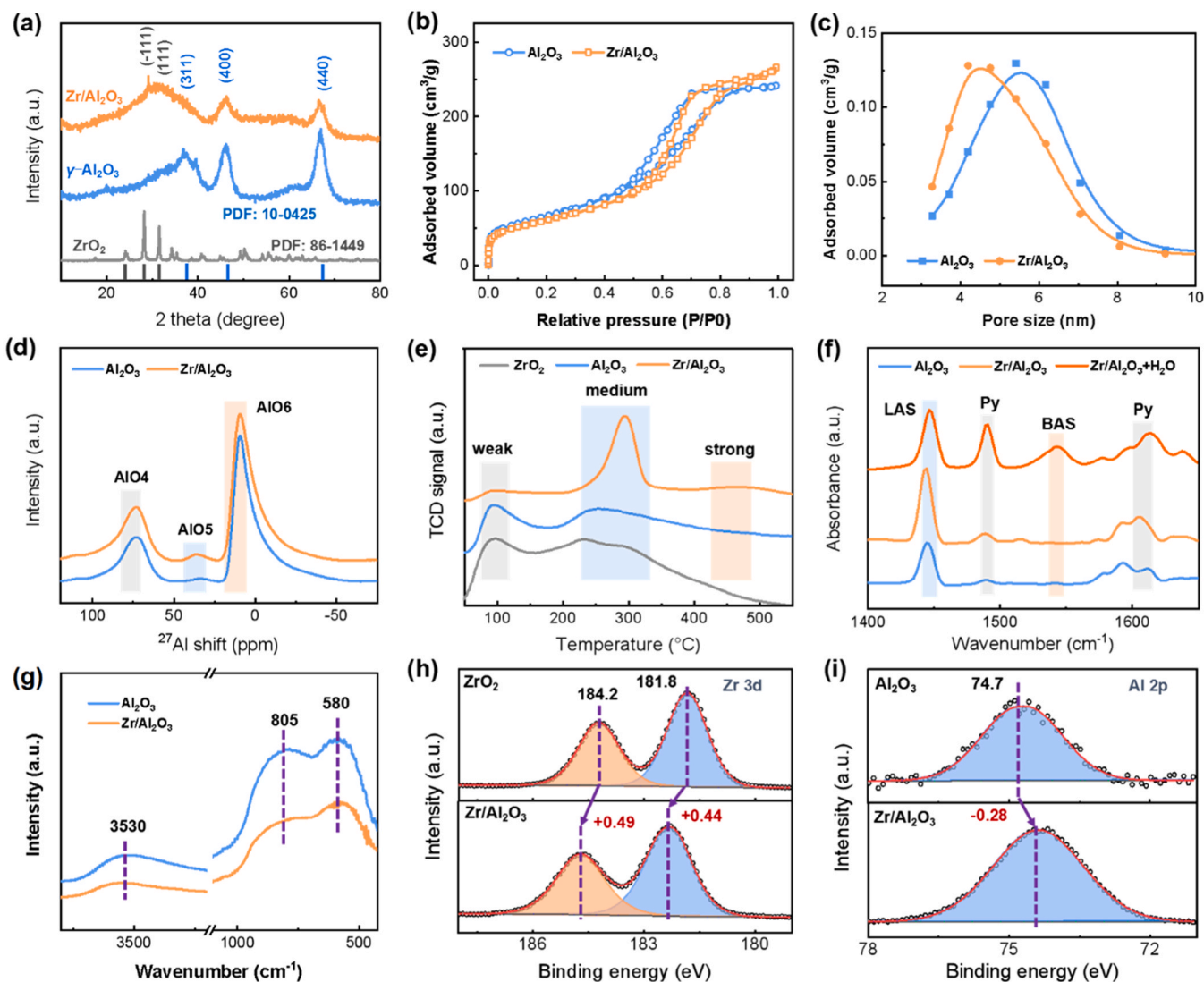

Fig. 2. Physical and chemical characterization of the as-prepared catalysts. (a) Powder wide-angle XRD pattern. (b-c) N$_2$ adsorption-desorption isotherms and pore size distribution. (d) ^{27}Al NMR spectra. (e) NH$_3$-TPD results. (f) Py-IR spectrum. (g) Powder IR spectra. (h-i) XPS spectra of Zr 3d and Al 2p.

support, leading to a noticeable change in specific surface area (from 240.6 to 213.8 m^2/g), pore volume (from 0.42 to 0.38 cm^3/g) and size distribution (from 8.1 to 5.4 nm) (Fig. 2c and Table S1). The ^{27}Al nuclear magnetic resonance (NMR) spectra (Fig. 2d) for γ-Al$_2$O$_3$ displayed resonances at 74, 35, and 9 ppm, corresponding to the AlO$_4$, AlO$_5$, and AlO$_6$ structural groups, respectively. In contrast, the NMR signals for the intrinsic AlO$_6$ coordination exhibited almost no change, while the signals of AlO$_4$ showed a significant increase. This increase suggests the generation of Al-O with unsaturated coordination [43].

Ammonia temperature-programmed desorption (NH$_3$-TPD) and pyridine-adsorption infrared (Py-IR) analysis were performed in tandem to investigate the properties of the surface acid sites. From the NH$_3$-TPD report (Fig. 2e) of the alumina support, two peaks were observed that can be assigned to weak (at 101.5 °C) and medium-strength (at 292.9 °C) acid sites with acid quantities of 0.21 and 0.25 mmol/g (Table S2), respectively. Similarly, the bare ZrO$_2$ nanoparticles presents two absorption peaks, while the medium-strength was also weak at 277.4 °C.

By contrast, the spectrum of Zr/Al$_2$O$_3$ exhibited more intense peaks, indicating medium-strength acid sites at 294.4 °C (0.54 mmol/g), surpassing those in the γ-Al$_2$O$_3$ spectrum. Additionally, a signal for strong acid sites at 437.1 °C (0.56 mmol/g) was detected for Zr/Al$_2$O$_3$. The total acid quantity of Zr/Al$_2$O$_3$ was 1.35 mmol/g, which is 1.93 times greater than that of pure Al$_2$O$_3$. The NH$_3$-TPD results also confirmed an increase in the density and strength of surface acids after the ZrO$_2$ coating. Furthermore, the Py-IR measurements (Fig. 2f) suggested that the absorption peak at 1450 cm^{-1} was contributed to the interaction of pyridine with unsaturated metal elements over surface (the LASs), while the peak at 1540 cm^{-1} was attributed to pyridine absorption on surface OH groups (the BASs). We assigned the IR signals at 1482 and 1580 cm^{-1} to the vibration of the pyridine ring and the C–H bond, respectively. At desorption temperature of 100 °C, almost exclusively LASs were observed on the alumina support, accounting for 98% of the total number of acid sites (136.6 μmol/g) (Table S3). Due to the metal-support interaction, the number of LASs increased to 186.8 μmol/g.
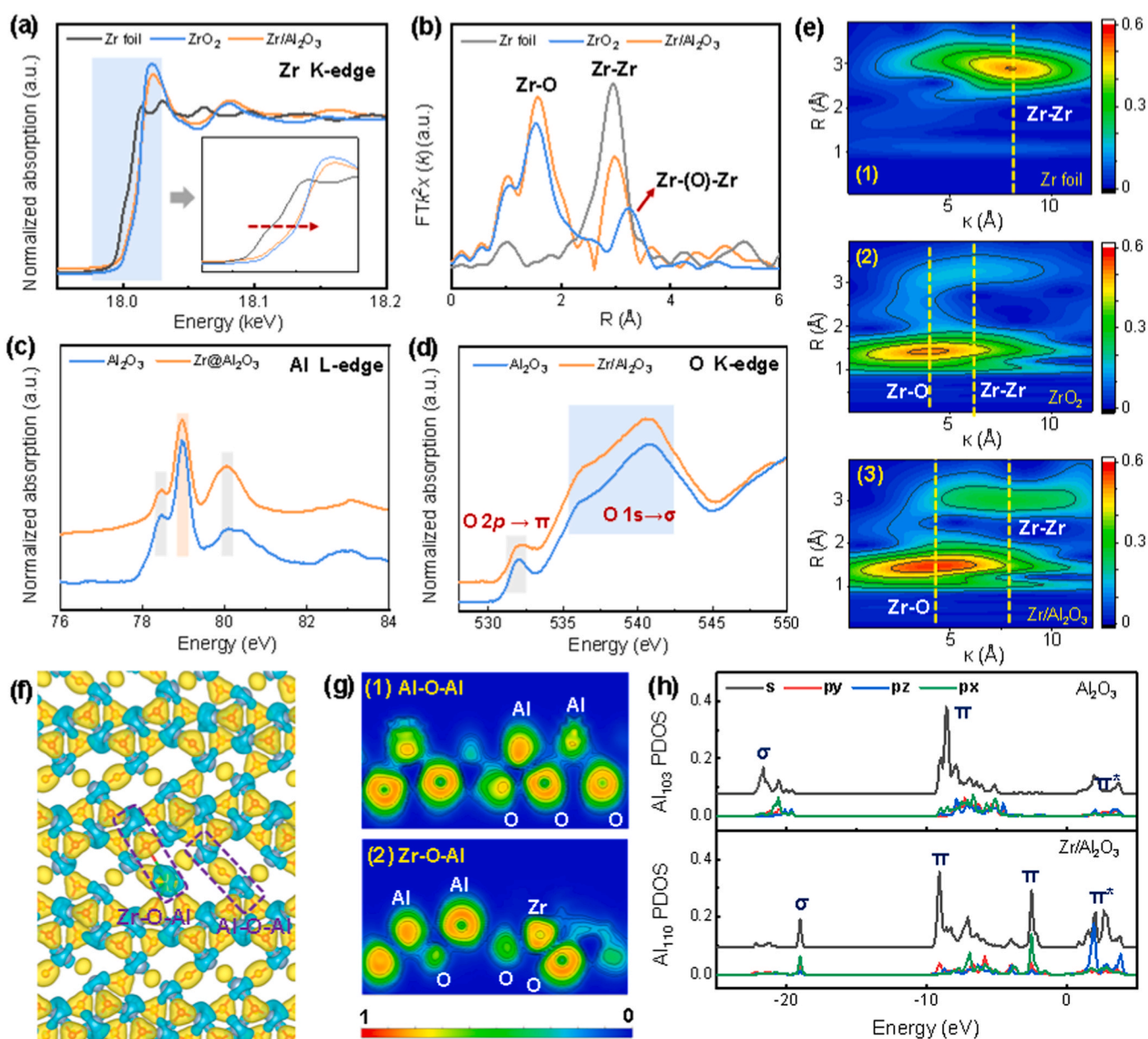

Fig. 3. Chemical coordination environment. (a) Normalized Zr K-edge XANES analysis. (b) EXAFS curve fitting in R space. (c) Al L-edge XAFS analysis. (d) O K-edge XAFS analysis. (e) Wavelet transform contour plots. (f) Charge density difference (charge accumulation in yellow and depletion in blue with an isosurface of 0.002 eV/Å). (g) ELF results. (h) Projected DOS for Al$_{102}$.

However, the catalyst still had relatively few BASs under the same measurement conditions. As the Zr/Al_2O_3 catalyst absorbed H_2O and pyridine, the strength of the IR signal of the BASs substantially increased to 61.4 μmol/g, and BASs constituted 67% of the total number of acid sites (153.6 μmol/g). In contrast, the number of LASs decreased to 92.2 μmol/g, suggesting that LASs could be transformed into BASs through the decomposition of H_2O over the catalyst. The infrared spectra of Al_2O_3 presented the IR peak at 805 cm^{-1} could be assigned to the vibration signal of Al-O-Al, which was weakened by the covered ZrO_2 clusters in Zr/Al_2O_3 catalyst (Fig. 2g).

The XPS survey showed that the Zr 3*d* XPS peaks at 181.8 and 184.2 electron volts (eV) in the Zr 3*d* spectra shifted positively by 0.44–0.49 eV (Fig. 2h), compared with bare ZrO_2 particles (50 nm). The Al 2*p* spectral peak (Fig. 2i) at 74.4 eV exhibited a negative shift (−0.28 eV), suggesting a change in metal-oxygen coordination. The XPS results for the metallic elements indicated that there was a higher electron density in the 2*p* orbit of Al, due to strong electrophilicity of Al-O bond. Accordingly, the Bader charge analysis referred valence electrons density of Al_{94} coordinated with Zr, is the greatest (1.83) among the marked Al atoms (Figure S5). In the O1s spectra (Figure S6), the peaks below 530 eV and around 531 eV were attributed to lattice oxygen in Zr–O and Al–O, respectively. The nearby peaks at binding energies of 531.5–531.8 and 530.5 eV corresponded to absorbed oxygen (O_{ads}, e.g., O^{2-}, O_2^{2-}, or O^-) and surface hydroxyls. The binding energy of Zr–O lattice oxygen was observed to decrease by 0.2 eV due to the influence of the metal–support interaction.

3.3. Coordination between metal and support

The Zr K-edge X-ray near-edge absorption spectroscopy (XANES) spectra collected (Fig. 3a) revealed that the fresh Zr/Al_2O_3 sample exhibited a strong white line, resembling zirconium oxide (ZrO_2). Further analysis of Fourier-transformed extended XAFS (EXAFS) spectra showed that the Zr–Zr peak in Zr foil, ZrO_2, and Zr/Al_2O_3 occurred at a similar distance of approximately 3.0 Å (Fig. 3b). The Zr–O and Zr–(O)–Zr peaks in the spectra of ZrO_2 and Zr/Al_2O_3 were situated at around 1.8 and 3.2 Å, respectively, which was not observed for the Zr foil. The EXAFS fitting for Zr/Al_2O_3 (Figure S7) indicated that two Zr atoms coordinated with 8–9 O atoms (Zr–O or Zr–O1 bond) with a slightly reduced bond length (Table S4), mainly ascribed to the decrease of charge density between Zr and O atoms. Moreover, the shorter bond length suggested the potential presence of Zr–O···Al bonds, indicating a strong interaction between the metal and the support material [44]. The Zr–Zr/Zr1 bonds in Zr/Al_2O_3 were similar to those in bulk ZrO_2. Aluminium L-edge XAFS (Fig. 3c) offered detailed bonding information (Al–O, and Al–O–Al) at 78–82 eV, and the intensity of these bonds was reduced by the presence of loaded Zr [45]. Oxygen K-edge XAFS (Fig. 3d) demonstrated antibonding states of O 2*p* hybridized with Al 3 *s*, 3*p*, and *sp* states, forming π^* and σ^* bonds. The zirconium $d3sp3$ states slightly enhanced the intensity of the σ^* bond. In Fig. 3e, wavelet transform contour plots of Zr K-edge weighted EXAFS spectra showed that both Zr–Zr and Zr–O coordination were present in the Zr/Al_2O_3 sample. The signal of the Zr–Zr bond was more pronounced when ZrO_2 was loaded onto the porous Al_2O_3.

Based on the structural characterization and analysis of coordination environments, DFT models were created as shown in Figure S8. The charge density difference plot for Zr/Al_2O_3 illustrated the charge transfer pattern around Zr–O–Al and Al–O–Al bonds (Fig. 3f). There was a noticeable increase in charge density between Al and O in the Zr–O–Al bond, resulting in a decrease in charge density between Zr and O. The electron transfer leaded to a strong interaction between ZrO_2 nanoparticles and the porous support. Electronic localization function (ELF) (Fig. 3g) indicated that covalent bonds were predominant between O and metal atoms. The degree of electron localization around Zr was slightly higher than around Al, suggesting a higher degree of delocalized electrons around Al. When comparing the projected DOS before and

after Zr loading (Fig. 3h), it was observed that the PDOS at –20 eV for Al–O significantly decreased after ZrO_2 loading. Additionally, a new bonding signal at –3 eV suggested that a covalent electron from ZrO_2 shifted towards the *p*- or *sp*-orbital electron of an Al atom. The π-bond around 9 eV remained relatively unchanged, possibly representing the bulk Al–O bond. Furthermore, the PDOS peaks at 2 eV could be attributed to the combination of antibonding orbital electrons of the π*-bond. Overall, the charge distribution scheme was in line with the experimental XPS and XAFS investigations.

3.4. Catalytic performance and reaction mechanism

Preliminary measurements were performed to screen the Zr/Al_2O_3 catalysts with various Zr/Al ratios. The results (Figure S9a) shown that the Zr/Al_2O_3 catalyst, containing 24.5% Zr by mass (with a Zr:Al molar ratio of 0.3, as per ICP measurements in Figure S9b), displayed the best CO_2 desorption performance. In fact, the strong oxide-support interaction was relatively weak, because of the insufficient Zr precursor. On the other hand, the confined zirconia nanoparticles over alumina support, leading to a decrease of specific surface area. Thus, the MPC effect on ZrO_2 particle size would be weakened with excess Zr precursor, resulted in relatively low Zr/Al contact area. Therefore, there was an optimal Zr/Al molar ratio for the Zr/Al_2O_3 catalysts, and the catalysts with 24.5% Zr was chosen for further evaluation. The rate of CO_2 desorption from the saturated MEA solvent at a specific heating profile (Fig. 4a, represented by the dotted line) with mesoporous γ-Al_2O_3 was slightly higher than the benchmark without a catalyst. The mixed metal oxides, due to the presence of ZrO_2 nanoparticles, performed even better. Furthermore, the maximum rate of CO_2 desorption from the CO_2-saturated MEA solvent with the Zr/Al_2O_3 catalyst reached 6.3 mmol/min as early as 17.5 min into the experiment (refer to Table S5). In contrast, the desorption rates for catalysts with and without γ-Al_2O_3 were only 3.67 and 3.2 mmol/min, respectively, at the same time point. Remarkably, using Zr/Al_2O_3 resulted in a 178% increase in the maximum desorption rate, with the corresponding desorption temperature dropping from 82.5 °C (at 22.4 min) to 77.5 °C (at 17.5 min) (Figure S10a).

The amount of CO_2 desorption (Fig. 4b), determined from the measured outlet concentration, significantly increased when a catalyst was employed. In particular, the use of the Zr/Al_2O_3 catalyst led to desorption of CO_2 (240 mmol within 120 min), which was 36.7% higher than the benchmark (176 mmol) and greater than when using pure Al_2O_3 (211 mmol), a mixture of ZrO_2 and Al_2O_3 (181 mmol) (Fig. 4b, insert). Power consumption measurements conducted during CO_2 desorption confirmed that using Zr/Al_2O_3 resulted in an approximately 27% lower heat duty compared to the catalyst-free case, while the heat duty reductions with γ-Al_2O_3 and a mixture of double oxides were 6.7% and 13.9%, respectively (Fig. 4c). In practical applications, complete regeneration of the solvent may not be cost-effective. For a target of 70% CO_2 desorption, there was a significant reduction in the desorption time compared to the catalyst-free benchmark, decreasing from 97.3 to 49.5 min. The five recycling tests showed no significant degradation in the catalytic performance of CO_2 desorption (Figure S10b).

The BCCAD system was activated and allowed to operate until it reached a stable condition using a simulated flue gas containing 11.7% CO_2 with the rest being N_2. The flow rates of the simulated flue gas and the circulating flow (containing 30 wt% MEA solvent) were maintained at 800 mL/min and 15 mL/min, respectively, resulting in a liquid-to-gas ratio of 18.75 L/m^3 (Figure S3). Further, 10 g pelletized Zr/Al_2O_3 was packed in a custom cylindrical container and placed in the 500-mL column for CO_2 desorption (Figure S4). Typical SEM/TEM images of the pelletized Zr/Al_2O_3 (Fig. 4d and Figure S11) show that some accumulations of ZrO_2 clusters observed on the Al support. From Fig. 4e, similar exposed surface of ZrO2 and Al2O3 was found as powder Zr/Al_2O_3, agreed with XRD results (Fig. 4f). To investigate the microstructure of the pelletized Zr/Al_2O_3, N_2 adsorption, and desorption, as well as TEM measurements, were performed. Compared to γ-Al_2O_3
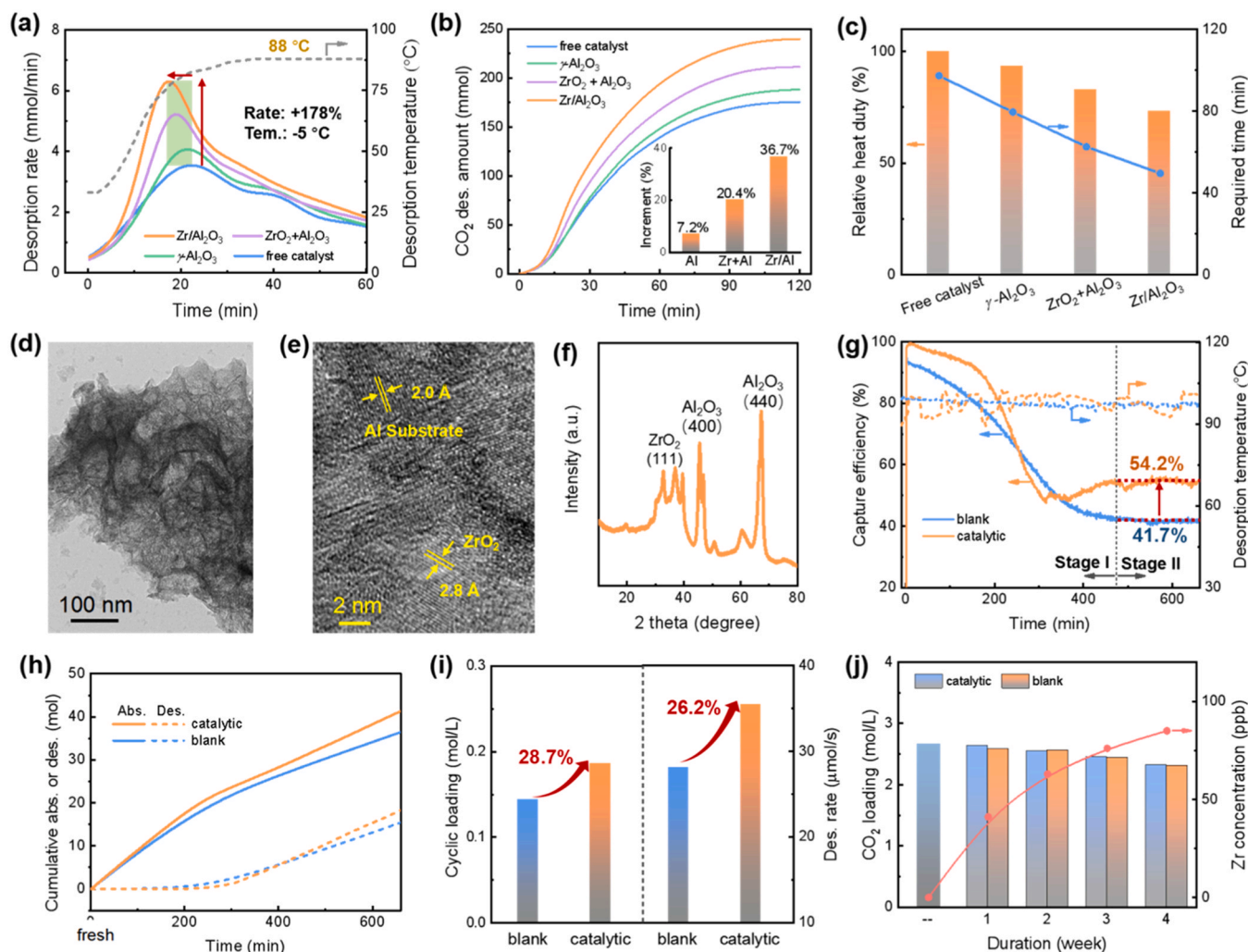
Fig. 4. Performance evaluation of catalytic CO_2 **desorption using Zr/Al$_2$O$_3$.** (a) CO_2 desorption rate and heating temperature profiles. (b) Amount of CO_2 desorbed within 120 min and the differences between catalysts (see insert). (c) Relative heat duty and required time for 70% desorption. (d-f) TEM images and XRD results of the pelletized Zr/Al$_2$O$_3$. (g) Profile of the CO_2 capture efficiency versus time. (h) Cumulative CO_2 absorption and desorption amounts. (i) Comparison of cyclic CO_2 loading and desorption rates. (j) CO_2 loading and Zr concentration in the spent solvent after long-term tests.

prepared using the template method, the commercial γ-Al$_2$O$_3$ sticks exhibited a lower specific surface area (209 m^2/g) (Figure S12). Type-IV isotherms were also observed, displaying a clear hysteresis loop, confirming the presence of mesoporosity in the support, similar to the powder Zr/Al$_2$O$_3$ catalysts. To make a comparison, we also conducted a similar experiment without adding the catalyst (referred to as the blank case) at this stage. The operating temperatures of the absorber and the heating of the rich solvent were controlled at 40.4 °C and 64.2 °C, respectively (Figure S13a). The CO_2 content in both the absorber and stripper was continuously monitored using an infrared (IR) flue gas analyzer, while the CO_2 loading of the solvent was determined through periodic sampling of the solvent.

Typically, it took approximately 420 min to reach a steady state of CO_2 absorption and desorption (Stage I), followed by a 240-min continuation (Stage II) (Figure S13b). During Stage I, the CO_2 capture efficiency gradually decreased due to the accumulation of carbamate in the lean solvent. In the first 200 min, the presence of Zr/Al$_2$O$_3$ resulted in a higher capture efficiency compared to the blank case. This was because the acid catalytic effect delayed the accumulation of carbamate, and the lean solvent maintained a high absorption capacity for CO_2. In Stage II, a balance between absorption and desorption was achieved, resulting in a capture efficiency of 54.2% with pelletized Zr/Al$_2$O$_3$, an increase of 12.5 percentage points compared to the blank case's 41.7%

(Fig. 4g). Additionally, the operational temperature showed more noticeable fluctuations (with an average value of 97.5 °C) compared to the blank case, likely due to bias flow in the catalyst package. After reaching stability, the CO_2 flow balance was well-maintained with an error of ±10% (Figure S13c), in comparison to the actual purging CO_2 flow of 92.7 mL/min, primarily attributed to measurement error. The total amount of absorbed and desorbed CO_2 exhibited a linear increase, and the difference stabilized at 22.9 and 21 moles in the presence and absence of catalysts, confirming the improvement brought about by pelletized Zr/Al$_2$O$_3$ (Fig. 4h). The reaction rate in the absorber and stripper became closer, at 35.5 and 28.1 μmol CO_2/s for the blank and catalytic cases (Figure S13d). There was a 26.2% increase in the desorption rate in the presence of catalysts, resulting in the cyclic CO_2 loading of the solvent increasing from 0.14 to 0.19 mol/L, indicating a more thorough regeneration with pelletized Zr/Al$_2$O$_3$ (Fig. 4i). After 11 h of testing, the white catalysts turned yellow (Figure S14), likely due to the absorption of amine-related species. After heat treatment at 500 °C, the surface area (211.7 m^2/g) and pore parameters showed no significant deterioration (Table S1). In a 4-week hydrothermal degradation test, the CO_2 loading of the MEA solvent in the presence of powder Zr/Al$_2$O$_3$ was comparable to that in its absence, suggesting that the catalysts had little impact on solvent degradation. Furthermore, the Zr ion concentration in the solvent remained at a low level (50–60 ppm),

indicating excellent durability of Zr/Al$_2$O$_3$, a critical requirement in practical applications (Fig. 4j).

3.5. Mechanism of catalytic carbamate decomposition by Zr/Al$_2$O$_3$

In practical applications, dealing with complex environments involving various gas-liquid multiphase flows and acid-base reactions in the stripper presents a significant challenge when it comes to tailoring catalytic materials with both high activity and stability. The Zr/Al$_2$O$_3$ catalysts were developed by combining two key factors: strong metal-oxide support interaction (SOSI) and the mesoporous confinement (MPC) effect, aimed at facilitating the catalytic regeneration of amine-based solvents (specifically, carbamate decomposition). We utilized mesoporous γ-Al$_2$O$_3$ with well-structured crystalline walls as a support for loading ZrO$_2$. The strong interaction between the oxide and the support provided a means to control the surface chemistry. More importantly, the confinement effect of Al$_2$O$_3$ concurrently restricted the growth of zirconium nanoclusters, thereby enhancing their stability.

A plausible reaction mechanism for the catalytic regeneration of solvents using Zr/Al$_2$O$_3$ was depicted in Fig. 5. On the Pauling scale, the Al atom (with an electronegativity of 1.61) was found to be more electronegative than the Zr atom (with an electronegativity of 1.33). This higher electronegativity of the Al atom led to an increased electron accumulation at the Al atom. Consequently, the resulting negative charge on oxygen could be balanced by metal cations or H$^+$, resulting in the stabilization of an OH group. Specifically, water molecules adsorbed on the catalyst could break down into surface hydroxyls, comprising terminal and bridging hydroxyls. As anticipated, the energy barrier for water dissociation was about 0.17 eV over Zr/Al$_2$O$_3$, which is notably lower compared to bare Al$_2$O$_3$ (as seen in Reaction I). The unsaturated coordination environment was favorable for the generation of hydroxyl groups, which subsequently served as acid catalysts in alkaline conditions [46,47]. The electron deficiency of Zr atoms was amplified due to the metal-support interaction, primarily attributed to the highly electronegative Al atoms [19]. As a result, the strong Zr-O interaction weakened or broke hydroxyl groups, thereby releasing H$^+$ into the solvent, acting as a Brønsted acid.

During the process of CO$_2$ absorption using MEA solvent, zwitterions

are initially formed, and these are promptly neutralized by a base (such as MEA, OH$^-$, or H$_2$O) to produce carbamates and protonated amines, as part of the exothermic reaction in line with the zwitterions theory (as seen in Reaction II). Upon continuous heating, the C-N bond of RNHCOO$^-$ and the N-H bond of RNH$_3^+$ weaken and break, and the H$^+$ replaces the C-N bond to create the MEA molecule (CO$_2$ decomposition). In the absence of a catalyst, the desorption temperature needs to exceed 120 °C for proper cyclic CO$_2$ loading. Hence, it is vital to overcome the limitations of alkaline solvents and establish an additional pathway for proton transfer. For Zr/Al$_2$O$_3$ catalysts, the surface hydroxyl groups, capable of both donating and accepting protons, significantly enhance reactions involving protonation and deprotonation (as observed in Reactions III and V). Proton transfer occurs on the catalyst's surface, involving a cycle between Brønsted acid and base sites. Consequently, the H$^+$ circulation within Zr/Al$_2$O$_3$ contributes to the decomposition of RNHCOO$^-$ and RNH$_3^+$, thereby accelerating the regeneration kinetics of the amine solvent.

4. Conclusions

In summary, we devised a method to create a honeycomb-like mesoporous γ-Al$_2$O$_3$ support with a straightforward soft template approach. This support effectively accommodates nano-scale ZrO$_2$ clusters, yielding a uniform distribution due to the mesoporous confinement effect. The strong interaction between the metal and support leads to the formation of stable active sites on the feasible solid acid catalyst, Zr/Al$_2$O$_3$. This unique combination of morphology and structural properties results in a coordination environment that offers a high surface area and abundant acid sites. The presence of Zr sites promotes the dissociation of adsorbed water and the generation of BAS, greatly expediting proton-involved reactions during CO$_2$ capture. Experimental results validated the outstanding performance of the catalyst with 24.5% Zr content. When using Zr/Al$_2$O$_3$, the maximum desorption rate reached 6.3 mmol/min, which was an impressive 178% higher than the benchmark catalyst-free system, resulting in a 27% reduction in relative heat duty. Furthermore, a bench-scale system was employed to comprehensively evaluate the performance of pelletized Zr/Al$_2$O$_3$, resulting in an increased capture efficiency of 54.2%, as opposed to the benchmark
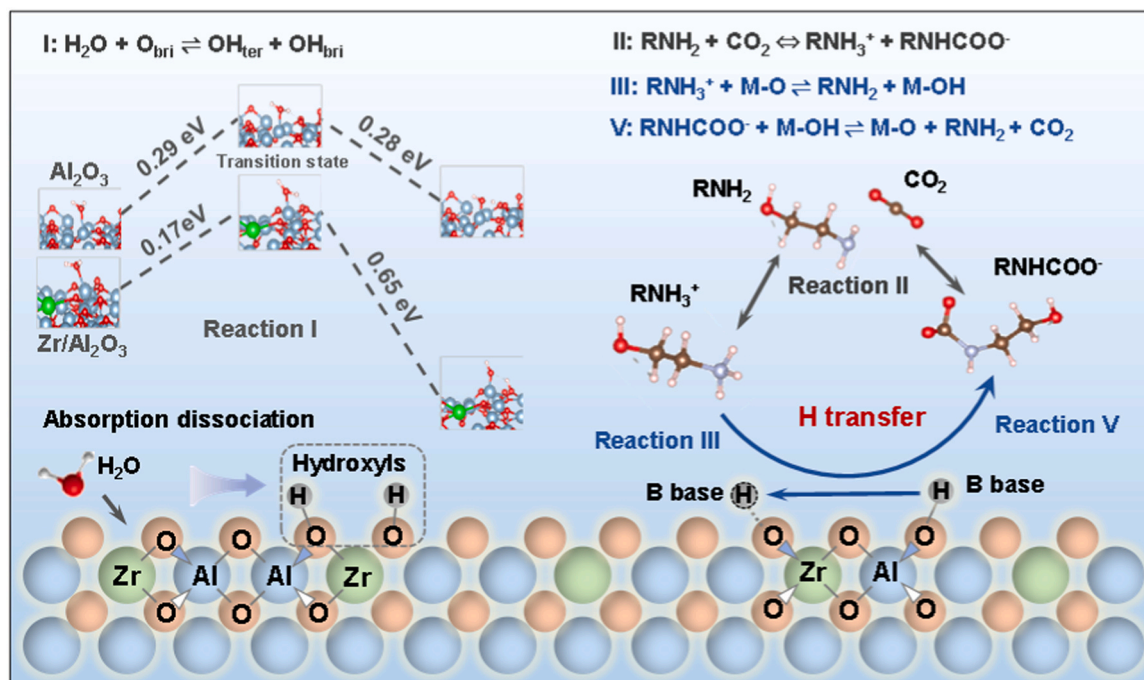

Fig. 5. Plausible reaction mechanism for catalytic solvent regeneration using Zr/Al$_2$O$_3$.

value of 41.7%. The durability of pelletized Zr/Al$_2$O$_3$ was demonstrated through an 11-h continuous test. This study opens up new avenues for the design of highly active and stable solid acid catalysts for low-cost industrial carbon capture.

Funding

CRediT authorship contribution statement

Junhua Li: Supervision, Funding acquisition. **Yue Peng:** Supervision. **Guoxiong Zhan:** Validation, Formal analysis, Data curation. **Zhoulan Huang:** Formal analysis, Data curation. **Xinhao Bai:** Formal analysis, Data curation. **Rong Wang:** Formal analysis, Data curation. **Zhen Chen:** Writing – review & editing, Methodology, Conceptualization. **Lei Xing:** Writing – review & editing, Methodology.

Declaration of Competing Interest

The authors declare that they have no known competing financial interests or personal relationships that could have appeared to influence the work reported in this paper.

Data availability

Data will be made available on request.

Appendix A. Supporting information

Supplementary data associated with this article can be found in the online version at doi:10.1016/j.apcatb.2024.124000.

References

[1] L. Rosa, D.L. Sanchez, M. Mazzotti, Assessment of carbon dioxide removal potential via BECCS in a carbon-neutral Europe, Energy Environ. Sci. 14 (2021) 3086–3097.
[2] R.F. Zheng, D. Barpaga, P.M. Mathias, D. Malhotra, P.K. Koech, Y. Jiang, M. Bhakta, M. Lail, A.V. Rayer, G.A. Whyatt, C.J. Freeman, A.J. Zwoster, K.K. Weitz, D.J. Heldebrant, A single-component water-lean post-combustion CO$_2$ capture solvent with exceptionally low operational heat and total costs of capture-comprehensive experimental and theoretical evaluation, Energy Environ. Sci. 13 (2020) 4106–4113.
[3] B.H. Lv, B.S. Guo, Z.M. Zhou, G.H. Jing, Mechanisms of CO$_2$ capture into monoethanolamine solution with different CO$_2$ loading during the absorption/desorption processes, Environ. Sci. Technol. 49 (2015) 10728–10735.
[4] E. Martin-Roberts, V. Scott, S. Flude, G. Johnson, R.S. Haszeldine, S. Gilfillan, Carbon capture and storage at the end of a lost decade, One Earth 4 (2021) 1569–1584.
[5] N.T. Yi, M.X. Fang, W.T. Di, Z.X. Xia, T. Wang, Q.H. Wang, Aerosol emissions of amine-based CO$_2$ absorption system: effects of condensation nuclei and operating conditions, Environ. Sci. Technol. 55 (2021) 5152–5160.
[6] X. Li, L. Xing, G. Zhan, Z. Huang, Z. Chen, H. Chang, J. Li, Oxygen vacancy enhanced proton transfer to boost carbamate decomposition kinetics with tunable heterostructure Ni/NiO, ACS Catal. 14 (2024) 1083–1092.
[7] Q.H. Lai, S. Toan, M.A. Assiri, H.G. Cheng, A.G. Russell, H. Adidharma, M. Radosz, M.H. Fan, Catalyst-TiO(OH)2 could drastically reduce the energy consumption of CO$_2$ capture, Nat. Commun. 9 (2018) 2672.
[8] X.B. Liu, X.W. Niu, G.X. Zhan, L. Xing, Z.L. Huang, B.L. Yuan, Y. Peng, Z. Chen, J.H. Li, Dynamic phase-splitting behaviour of biphasic solvent for carbon capture in a novel annular phase separator, Appl. Energy 360 (2024) 122788.
[9] J.X. Ye, C.K. Jiang, H. Chen, Y. Shen, S.H. Zhang, L.D. Wang, J.M. Chen, Novel biphasic solvent with tunable phase separation for CO$_2$ capture: role of water content in mechanism, kinetics, and energy penalty, Environ. Sci. Technol. 53 (2019) 4470–4479.
[10] Y.C. Li, Z. Chen, G.X. Zhan, B.L. Yuan, L.D. Wang, J.H. Li, Inducing efficient proton transfer through Fe/Ni@COF to promote amine-based solvent regeneration for

[11] achieving low-cost capture of CO$_2$ from industrial flue gas, Sep. Purif. Technol. 298 (2022).
[11] U.H. Bhatti, S. Nam, S. Park, I.H. Baek, Performance and mechanism of metal oxide catalyst-aided amine solvent regeneration, ACS Sustain. Chem. Eng. 6 (2018) 12079–12087.
[12] X.W. Zhang, S.S. Zhang, Z. Tan, S.S. Zhao, Y. Peng, C. Xiang, W.B. Zhao, R. Zhang, One-step synthesis of efficient manganese-based oxide catalyst for ultra-rapid CO$_2$ absorption in MDEA solutions, Chem. Eng. J. 465 (2023) 142878.
[13] B.L. Yuan, G.X. Zhan, Z. Chen, Y.C. Li, L.D. Wang, C.F. You, J.H. Li, Intrinsic insight of energy-efficiency optimization for CO$_2$ capture by amine-based solvent: effect of mass transfer and solvent regeneration, Int. J. Greenh. Gas Control 118 (2022) 103673.
[14] B.L. Yuan, G.X. Zhan, L. Xing, Y.C. Li, Z.L. Huang, Z. Chen, L.D. Wang, J.H. Li, Boosting CO$_2$ absorption and desorption of biphasic solvent by nanoparticles for efficient carbon dioxide capture, Sep. Purif. Technol. 329 (2024) 125108.
[15] X.M. Wu, H.F. Fan, Y.H. Mao, M. Sharif, Y.S. Yu, Z.X. Zhang, G.X. Liu, Systematic study of an energy efficient MEA-based electrochemical CO$_2$ capture process: from mechanism to practical application, Appl. Energy 327 (2022) 120014.
[16] Z. Chen, B.L. Yuan, G.X. Zhan, Y.C. Li, J.Y. Li, J.J. Chen, Y. Peng, L.D. Wang, C.F. You, J.H. Li, Energy-efficient biphasic solvents for industrial carbon capture: role of physical solvents on CO$_2$ absorption and phase splitting, Environ. Sci. Technol. 56 (2022) 13305–13313.
[17] F.Z. Meng, Y. Meng, T.Y. Ju, S.Y. Han, L. Lin, J.G. Jiang, Research progress of aqueous amine solution for CO$_2$ capture: a review, Renew. Sustain. Energy Rev. 168 (2022) 112902.
[18] M.S. Alivand, O. Mazaheri, Y. Wu, A. Zavabeti, A.J. Christofferson, N. Meftahi, S.P. Russo, G.W. Stevens, C.A. Scholes, K.A. Mumford, Engineered assembly of water-dispersible nanocatalysts enables low-cost and green CO$_2$ capture, Nat. Commun. 13 (2022) 1249.
[19] C. Zhou, I. Khalil, F. Rammal, M. Dusselier, P. Kumar, M. Lacroix, E. Makshina, Y.H. Liao, B.F. Sels, A critical revisit of zeolites for CO$_2$ desorption in primary amine solution argues its genuine catalytic function, ACS Catal. 12 (2022) 11485–11493.
[20] X.W. Zhang, Z.Q. Zhu, X.Y. Sun, J. Yang, H.X. Gao, Y.Q. Huang, X. Luo, Z.W. Liang, P. Tontiwachwuthikul, Reducing energy penalty of CO$_2$ capture using Fe promoted SO42-/ZrO$_2$/MCM-41 catalyst, Environ. Sci. Technol. 53 (2019) 6094–6102.
[21] K.L. Xue, G.X. Zhan, X.A. Wu, H. Zhang, Z. Chen, H.P. Chen, J.H. Li, Integration of membrane contactors and catalytic solvent regeneration for efficient carbon dioxide capture, J. Membr. Sci. 684 (2023) 121870.
[22] L. Xing, K.X. Wei, Q.W. Li, R.J. Wang, S.H. Zhang, L.D. Wang, One-step synthesized SO$_4^{2-}$/ZrO$_2$-HZSM-5 solid acid catalyst for carbamate decomposition in CO$_2$ capture, Environ. Sci. Technol. 54 (2020) 13944–13952.
[23] L. Xing, Z. Chen, G.X. Zhan, Z.L. Huang, M.Y. Li, Y.C. Li, L.D. Wang, J.H. Li, Sulfur migration enhanced proton-coupled electron transfer for efficient CO$_2$ desorption with core-shelled C@Mn$_3$O$_4$, Environ. Sci. Technol. 58 (2024) 4606–4616.
[24] H.X. Gao, Y.F. Huang, X.W. Zhang, Z.A.S. Bairq, Y.Q. Huang, P. Tontiwachwuthikul, Z.W. Liang, Catalytic performance and mechanism of SO$_4^{2-}$/ZrO$_2$/SBA-15 catalyst for CO$_2$ desorption in CO$_2$-loaded monoethanolamine solution, Appl. Energy 259 (2020) 114179.
[25] G.Q. Li, D. Zhang, Y.F. Yu, S.Y. Huang, W.T. Yang, L.Y. Cao, Activating MoS$_2$ for pH-universal hydrogen evolution catalysis, J. Am. Chem. Soc. 139 (2017) 16194–16200.
[26] M.Y. Li, L. Xing, Z.F. Xu, Z.W. Liang, T.Y. Qi, Y.C. Li, S.H. Zhang, L.D. Wang, Embedded Mo/Mn atomic regulation for durable acidity-reinforced HZSM-5 catalyst toward energy-efficient amine regeneration, Environ. Sci. Technol. 57 (2023) 15465–15474.
[27] J.H. Lin, C.P. Ma, Q. Wang, Y.F. Xu, G.Y. Ma, J. Wang, H.T. Wang, C.L. Dong, C.H. Zhang, M.Y. Ding, Enhanced low-temperature performance of CO$_2$ methanation over mesoporous Ni/Al$_2$O$_3$-ZrO$_2$ catalysts, Appl. Catal. B-Environ. 243 (2019) 262–272.
[28] K. Wang, H.Z. Tian, S.B. Hua, C.Y. Zhu, J.J. Gao, Y.F. Xue, J.M. Hao, Y. Wang, J.R. Zhou, A comprehensive emission inventory of multiple air pollutants from iron and steel industry in China: temporal trends and spatial variation characteristics, Sci. Total Environ. 559 (2016) 7–14.
[29] C.Y. Liu, Y.H. Zhang, F. Dong, A.H. Reshak, L.Q. Ye, N. Pinna, C. Zeng, T.R. Zhang, H.W. Huang, Chlorine intercalation in graphitic carbon nitride for efficient photocatalysis, Appl. Catal. B-Environ. 203 (2017) 465–474.
[30] L.L. Xu, J. Zhang, F.G. Wang, K.D. Yuan, L.J. Wang, K. Wu, G.Q. Xu, W. Chen, One-step synthesis of ordered mesoporous CoAl$_2$O$_4$ spinel-based metal oxides for CO$_2$ reforming of CH$_4$, RSC Adv. 5 (2015) 48256–48268.
[31] C.Y. Lin, D.T. Zhang, Z.H. Zhao, Z.H. Xia, Covalent organic framework electrocatalysts for clean energy conversion, Adv. Mater. 30 (2018) 1703646.
[32] X.F. Ma, Y. Xiong, Y.S. Liu, J.Q. Han, G.G. Duan, Y.M. Chen, S.J. He, C.T. Mei, S.H. Jiang, K. Zhang, When MOFs meet wood: from opportunities toward applications, Chem 8 (2022) 2342–2361.
[33] I. Abbas, H. Kim, C.H. Shin, S. Yoon, K.D. Jung, Differences in bifunctionality of ZnO and ZrO$_2$ in Cu/ZnO/ZrO$_2$/Al$_2$O$_3$ catalysts in hydrogenation of carbon oxides for methanol synthesis, Appl. Catal. B-Environ. 258 (2019) 117971.
[34] D.Q. Zhang, A.J. Duan, Z. Zhao, C.M. Xu, Synthesis, characterization, and catalytic performance of NiMo catalysts supported on hierarchically porous Beta-KIT-6 material in the hydrodesulfurization of dibenzothiophene, J. Catal. 274 (2010) 273–286.
[35] H. Wang, L. Wang, D. Lin, X. Feng, Y.M. Niu, B.S. Zhang, F.S. Xiao, Strong metal-support interactions on gold nanoparticle catalysts achieved through Le Chatelier's principle, Nat. Catal. 4 (2021) 418–424.

[36] J. Zhang, H. Wang, L. Wang, S. Ali, C.T. Wang, L.X. Wang, X.J. Meng, B. Li, D.S. Su, F.S. Xiao, Wet-chemistry strong metal-support interactions in titania-supported Au catalysts, J. Am. Chem. Soc. 141 (2019) 2975–2983.

[37] Z. Chen, H.B. Yin, C.Z. Wang, R. Wang, Y. Peng, C.F. You, J.H. Li, New insights on competitive adsorption of NO/SO_2 on TiO_2 anatase for photocatalytic NO oxidation, Environ. Sci. Technol. 55 (2021) 9285–9292.

[38] Q. Yuan, A.X. Yin, C. Luo, L.D. Sun, Y.W. Zhang, W.T. Duan, H.C. Liu, C.H. Yan, Facile synthesis for ordered mesoporous gamma-aluminas with high thermal stability, J. Am. Chem. Soc. 130 (2008) 3465–3472.

[39] Q. Yuan, H.H. Duan, L.L. Li, Z.X. Li, W.T. Duan, L.S. Zhang, W.G. Song, C.H. Yan, Homogeneously dispersed ceria nanocatalyst stabilized with ordered mesoporous alumina, Adv. Mater. 22 (2010) 1475–1478.

[40] Z.X. Wu, Q.A. Li, D. Peng, P.A. Webley, D.Y. Zhao, Ordered mesoporous crystalline gamma-Al_2O_3 with variable architecture and porosity from a single hard template, J. Am. Chem. Soc. 132 (2010) 12042–12050.

[41] B. Ashford, Y. Wang, C.-K. Poh, L. Chen, X. Tu, Plasma-catalytic conversion of CO_2 to CO over binary metal oxide catalysts at low temperatures, Appl. Catal. B: Environ. 276 (2020) 119110.

[42] J. Ni, W. Leng, J. Mao, J. Wang, J. Lin, D. Jiang, X. Li, Tuning electron density of metal nickel by support defects in Ni/ZrO_2 for selective hydrogenation of fatty acids to alkanes and alcohols, Appl. Catal. B: Environ. 253 (2019) 170–178.

[43] R. Lizarraga, E. Holmstroem, S.C. Parker, C. Arrouvel, Structural characterization of amorphous alumina and its polymorphs from first-principles XPS and NMR calculations, Phys. Rev. B 83 (2011) 094201.

[44] H.M. Liu, H. Wang, Z.W. Liu, H.J. Ling, C.F. Zhou, H.W. Li, C. Stampfl, X.Z. Liao, J. L. Wang, X.H. Shi, J. Huang, Confinement impact for the dynamics of supported metal nanocatalyst, Small 14 (2018) 1801586.

[45] Z.Q. Wang, C.L. Li, L.J. Liu, T.K. Sham, Probing defect emissions in bulk, micro- and nano-sized α-Al2O3 via X-ray excited optical luminescence, J. Chem. Phys. 138 (2013) 084706.

[46] L. Mino, A. Morales-Garcia, S.T. Bromley, F. Illas, Understanding the nature and location of hydroxyl groups on hydrated titania nanoparticles, Nanoscale 13 (2021) 6577–6585.

[47] L.Y. Ding, M. Li, Y.K. Zhao, H.N. Zhang, J.T. Shang, J.B. Zhong, H. Sheng, C. C. Chen, J.C. Zhao, The vital role of surface Bronsted acid/base sites for the photocatalytic formation of free center dot OH radicals, Appl. Catal. B-Environ. 266 (2020) 118634.